King Saud University

Arabian Journal of Chemistry

www.ksu.edu.sa
www.sciencedirect.com

ORIGINAL ARTICLE

Part I: Ni-Co alloy foils electrodeposited using ionic liquids

Inam M.A. Omar [a,b], Madzlan Aziz [b], Khadijah M. Emran [a],*

[a] *Chemistry Department, College of Science, Taibah University, AlMaddinah Al Mounwara, Saudi Arabia*
[b] *Department of Chemistry, Faculty of Science, Universiti Teknologi Malaysia, 81310 Johor Bahru, Johor, Malaysia*

Abstract   The Ni-Co alloy co-electrodeposit from a sulfate bath including two new ionic liquids 1-methyl-3-(2-oxo-2-((2,4,5 trifluorophenyl) amino) ethyl)-1H-imidazol-3-ium iodide [MOFIM]I and 1-(4-fluorobenzyl)-3-(4-phenoxybutyl) imidazol-3-ium bromide [FPIM]Br as additives was characterized using the SEM, EDS, EDS mapping, XRD, AFM and microhardness measurement techniques. The resultant surface morphologies in acidic sulfate baths on a copper substrate demonstrated that both the [MOFIM]I and [FPIM]Br additives served as effective leveling agents. The Ni-Co alloy co-deposit morphology in the [MOFIM]I bath was more enhanced (non-grained coating, R_a of 28 nm and R_t of 35.5 nm) than that in the [FPIM]Br bath (grain size 225 nm, R_a of 51. 1 nm and R_t of 65.7 nm) owing to the molecular structure. The co-deposition of Co and Ni from the acidic baths was of the anomalous type. Moreover, the anomalous behavior of the Ni-Co co-deposition was alleviated after [MOFIM]I and [FPIM]Br were introduced in the bath. To determine the optimal bath conditions, the cathodic current efficiency (CCE%) value was calculated during the Ni-Co alloy co-electrodeposition process under three different compositions and different operating conditions. Under the composition of Ni 70% and Co 30% (Ni70%-Co30% alloy deposit), the CCE% values increased considerably, with maximum values of 99.8% and 97.07% in the baths including [MOFIM]I and [FPIM]Br, respectively.

1. Introduction

Nickel (Ni)-cobalt (Co) alloys exhibit desirable magnetic, mechanical, chemical, physical, and thermophysical characteristics, including wear resistance, high thermal conductivity, high hardness, and superior corrosion resistance. Owing to their electrocatalytic properties, Ni-Co alloys (Al Radadi and Ibrahim, 2020; El-Feky et al., 2013; Lupi et al., 2017; Chai and Jiang, 2019) are widely used in several industrial applications, such as electronics, computers, automotive devices, and energy storage devices, especially under environments that

* Corresponding author.
  E-mail addresses: Emomar@taibahu.edu.sa (I.M.A. Omar), madzlan@utm.my (M. Aziz), kabdalsamad@taibahu.edu.sa (K.M. Emran).
Peer review under responsibility of King Saud University.

ELSEVIER **Production and hosting by Elsevier**

require the devices to be heat and corrosion resistant (Al Radadi and Ibrahim, 2020; Al Raddadi, 2014). Electrodeposition is a promising technique to obtain Ni-Co alloys, as the associated cost is low, device maintenance is convenient, a uniform coating thickness can be obtained, and complex geometries can be handled with a low toxicity (Al Radadi and Ibrahim, 2020). Several researchers have investigated the characteristics of Ni-Co alloy coatings obtained from different baths (Al Radadi and Ibrahim, 2020; Vijayakumar et al., 2013; Tian et al., 2011) including or not including additives (El-Feky et al., 2013; Vijayakumar et al., 2013; Nemţoi et al., 2009). However, the use of an acid sulfate bath is becoming increasingly popular as it is relatively inexpensive, safe, and nonpolluting (Loto, 2012) and can help obtain smooth and fine surfaces (El-Feky et al., 2013). With the rapid development in science and technology, material property requirements have become more stringent. Recent techniques to prepare composite coatings involve the use of additives to realize specific applications of the materials. Additives are widely used in electrodeposition baths as they influence the growth, morphology and structure of the resulting deposits. In general, additives are added to plating solvents to improve the properties of the electrodeposit, such as the grain size, brightness, internal stress, hardness and resistance to corrosion (El-Feky et al., 2013; Jamil et al., 2017; Alesary et al., 2019). The additives are often incorporated in the deposit (Omar, 2012), and they inhibit the crystal growth toward other crystallographic axes (Hamilakis et al., 2015; Hashemi et al., 2017) as they are adsorbed on the plated surface. However, Ni, Co or Ni-Co alloys electrodeposited from baths including additives have been noted to exhibit a granular coating with extensive microcracking on the surface (Al Raddadi, 2014; Ji et al., 2016), low hardness and yield strength (Zamani et al., 2016), low corrosion resistance (Cârâc and Ispas, 2012), and low cathodic current efficiency (Lupi et al., 2017; Al Raddadi, 2014) under a high temperature and current density. Consequently, certain environmentally unfriendly materials such as Cd^{2+} compounds (Mohanty et al., 2002); thiourea (Zhu et al., 2012), or additives with a high flammability, high volatility (Zhu et al., 2012), easy decomposition (Ibrahim and Omar, 2013), and low thermal stability (Qibo and Yixin, 2017) have been used. In this regard, ionic liquids (ILs) represent a promising alternative chemical group for many existing materials to be used in electrodeposition due to their excellent properties (Yao et al., 2019; Ibrahim et al., 2016; Anicai et al., 2011). Ionic liquids (ILs) are molten salts with melting points below 100 °C and they consist solely of cations and anions. The charge on these ions is delocalized or shielded by side groups, which is one reason why the melting points of ionic liquids are remarkably low (Barbato, 2009). ILs are usually large electrochemical windows: The most important advantage of ILs is their large electrochemical windows (> 5V) which gives access to elements that cannot be electrodeposited from aqueous or organic solutions such as for example, Al, Mg, Ti and Ta, at moderate temperatures. The effect of cation and anion: Generally, the cation controls the physical properties of the salt such as its structure and morphology and the anion affects the stability and chemical reactivity. Moreover, the anion affects coordination geometry around the metal ion which effects reduction potential, reduction current and nucleation. Both the anion and cation affect the conductivity and viscosity. Properties of ILs, such as dissolving ability from metal salts,

polarity, viscosity and density can be tuned by an appropriate choice of the anion and the cation. Overall, ionic liquids are inevitably advanced, technological solvents that can be designed to fit a particular application. Conductivity: ILs have reasonably good ionic conductivities, between 10^{-3} and 10^{-2} $\Omega^{-1}\,cm^{-1}$, compared with those of organic solvents/electrolyte systems. These conductivities make ionic liquids interesting solvents for low-temperature electrodeposition studies. Low vapor pressures: most ILs have at or near room temperature vapor pressures of 10^{-11}–10^{-10} mbar allowing experiments to be done at temperatures up to 400 °C. The very small vapor pressure of ILs also allows their use in vacuum experiments even at elevated temperatures. Thermal stability: ILs can be used at wider temperature ranges and still have great thermal control of electrochemical processes, unlike when using conventional molecular solvent/electrolyte systems. Less toxic: from the environmental perspective ILs are environmentally cleaner than other media. When used in electroplating processes, strongly aqueous electrolytes create quantities of metal-laden, corrosive effluent solution, whereas in ILs electrolytes the metals will precipitate and be readily separated and recycled. Good solvents for both organics and inorganics: metal ion electrodeposition potentials are much closer together in ILs compared with water, enabling easier preparation of alloys and the possibility of a much wider range of possible electroplated alloys, which are difficult or impossible in water (Yao et al., 2019; Ibrahim et al., 2016; Anicai et al., 2011). Many researchers have used ILs to prepare an electroplating bath (Alesary et al., 2019; Costovici et al., 2016; Ismail, 2017). However, relatively few studies have investigated the role of ILs as additives in the electrodeposition processes (Allahyarzadeh et al., 2011; Qibo and Yixin, 2017). This means that study the effect of ILs as additives during electrodeposition process is insufficient. Therefore, in the current work, the effect of two novel synthesized ILs, namely, 1-methyl-3-(2-oxo-2-((2,4,5 trifluorophenyl) amino) ethyle)-1H-imidazol-3-ium iodide ([MOFIM]I) and 1-(4-fluorobenzyl)-3-(4-phenoxybutyl)imidazol-3-ium bromide ([FPIM]Br) on the Ni-Co alloy coatings generated from a sulfate bath was studied for the first time as new ionic liquid addition agents in Ni-Co alloy electrodeposition and compared. The structures, morphologies, and compositions of the Ni-Co alloy coatings were determined using a scanning electron microscope (SEM) combined with the energy dispersive X-ray spectroscopy (EDS), EDS mapping, X-ray diffraction (XRD) and atomic force microscopy (AFM) techniques.

2. Experimental details

2.1. Composition of the electrodeposition baths

The Ni-Co alloy was electrochemically codeposited onto a Cu substrate by using an acidic sulfate bath under three different compositions of $[Ni^{2+}]$ and $[Co^{2+}]$, without and with [MOFIM]I and [FPIM]Br, as summarized in Table 1. All the chemicals and reagents were analytical grade, and the electrolytes were freshly prepared using doubly distilled water. The pH was adjusted using 1:1 ($H_2SO_4:H_2O$) and measured using a pH meter (HANNA, IH 2210, ITALY). The role of boric acid in the electrolyte is as buffer to keep pH of bath constant during electrodeposition.

Table 1 The bath composition, optimum conditions and electrodes using for co-electrodeposition of Ni-Co alloy.

Bath composition g/L (Mohanty et al., 2002)	Ni70%-Co30%			Ni50%-Co50%			Ni30%-Co70%		
	Bath1	Bath2	Bath3	Bath4	Bath5	Bath6	Bath7	Bath8	Bath9
[NiSO$_4$·6H$_2$O]	70	70	70	50	50	50	30	30	30
[CoSO$_4$·7H$_2$O]	30	30	30	50	50	50	70	70	70
[H$_3$BO$_3$]	**30**	**30**	**30**	**30**	**30**	**30**	**30**	**30**	**30**
[MOFIM]I	0	1×10^{-5}	0	0	1×10^{-5}	0	0	1×10^{-5}	0
[FPIM]Br	0	0	1×10^{-5}	0	0	1×10^{-5}	0	0	1×10^{-5}

Optimum conditions	
Current density (mA/cm^2)	20
pH	4.5
Temperature (°C)	25
Deposit time (min)	10

Electrodes	
Cathode	Cu sheet (6.25 cm^2, 0.25 cm thick, 99.99%, Advent Research Materials)
Anode	Pt sheet 6.25 cm^2, 0.25 cm thick, 99.95% metals basis. Alfa Aeser.
Working electrode (WE)	Glassy carbon electrode (GCE) (0.156 cm^2 Glassy carbon disk electrode in peek body 6 mm Reorder ET 051)
Counter electrode (CE)	Pt sheet 6.25 cm^2, 0.25 cm thick, 99.95% metals basis. Alfa Aeser.
Reference electrode (RE)	Saturated calomel electrode (SCE), (Hanna Instrument (Italy) HI5412)
The deposition cell	A rectangular trough (10× 2.5× 2 cm, made by Perspex).

2.2. Additive preparation

The imidazolium iodide incorporating an aromatic amide, namely, 1-methyl-3-(2-oxo-2-((2,4,5-trifluorophenyl) amino) ethyl)-1H-imidazol-3-ium iodide (MOFIM]I), M.W = 397.15 g/mol, was synthesized through simple quaternization of methylimidazole with fluorinated aromatic acetamide bromide in acetonitrile (Rezki et al., 2020; Omar et al., 2020), as shown in Fig. 1a. The imidazolium bromide incorporating an aromatic amide, namely, 1-(4-fluorobenzyl)-3-(4-phenoxybutyl)i midazol-3-ium bromide ([FPIM]Br), as shown in Fig. 1b, M. W = 405.31 g/mol, was synthesized using ultrasonic irradiation, as reported in Omar et al. (2020). Both studied ILs soluble in warm aqueous solution (50–60 °C).

2.3. Electrochemical setup

The co-electrodeposition of the Ni-Co alloy was carried out cathodically on a Cu substrate flat sheet, and a platinum (Pt) sheet with the same dimensions was used as the anode, as described in Table 1. Before each experiment, the Cu sheets were cleaned in pickling solution (300 ml H2SO4, 100 ml HNO3, 5 ml HCl and 595 ml H2O) (Omar et al., 2020) for 20 s; subsequently, the sheets were rinsed with distilled water and dried in a desiccator. The cathodic current efficiency (CCE%) of the Ni-Co alloy co-electrodeposition was determined by supplying direct current using a DC power supply unit (QJ3005A) under the different conditions described in Table 1. The Ni and Co composite coatings were obtained using Cu and Pt sheets as the cathode and anode, respectively. The CCE% was calculated using the approach described in Al Raddadi (2014) as following:

The partial current efficiencies of the parent metals in the alloy CCE$_{Ni}$ % and CCE$_{Co}$ % were determined from the relations:

$$CCE_{Ni}\% = \frac{WNi}{Wt} \times 100 \qquad (1)$$

$$CCE_{Co}\% = \frac{WCo}{Wt} \times 100 \qquad (2)$$

where w$_{Ni}$ is the practical weight of the nickel deposit, w$_{Co}$ is the practical weight of the cobalt deposit and w$_t$ is the theoret-
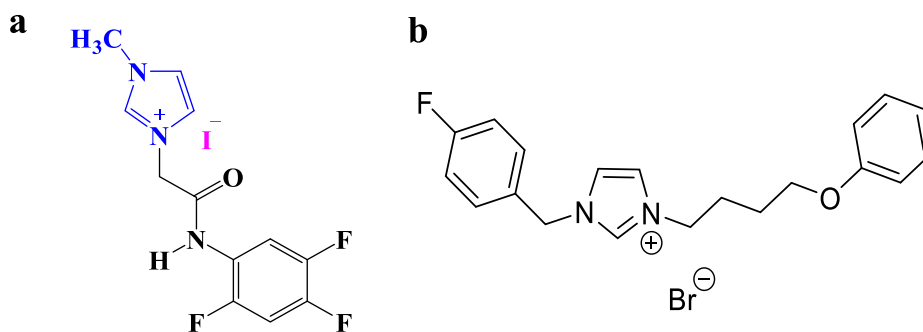

Fig. 1 The molecular structure of the ionic liquids namely (a) 1-methyl-3-(2-oxo-2-((2,4,5 trifluorophenyl)amino)ethyle)-1H-imidazol-3-ium iodide ([MOFIM]I), (b) 1-(4-fluorobenzyl)-3-(4-phenoxybutyl)imidazol-3-ium bromide ([FPIM]Br).

ical weight of the deposit calculated using Faraday's low. Then, the total efficiency of the alloy is equal to the sum of CCE_{Ni} % and CCE_{Co}%.

$$CCE_{alloy} = CCE_{Ni}\% + CCE_{Co}\% \tag{3}$$

The practical current efficiency of the parent metals in an alloy $CCE\%_{Ni}$ and $CCE_{Co}\%$ are obtained from the composition of the alloy. The composition of the alloy is determined by energy dispersive X-ray spectroscopy (EDS) analysis tool attached to Scanning electron microscopy (SEM).

2.4. Characterization

Morphological tests of the Ni-Co alloy thin films were performed using a scanning electron microscope (SEM, JEOL JSM-6000, Shimadzu, Japan) integrated with an energy dispersed X-ray spectrometer (EDS) microanalysis hardware with an accelerating voltage of 15 kV. The phase of the prepared Ni-Co alloy films was identified using an X-ray diffraction (XRD, Shimadzu, XRD-7000, Japan) analyzer using monochromatic Cu kα radiation (k = 1.5406 A°), operated at 40 kV and 30 mA at a 2θ angle pattern. The topography of the deposited layers of the Ni70-Co30 alloy and the roughness were evaluated using an atomic force microscopy (AFM, Veeco digital instrument CP-II(contact mode). A Vickers microhardness (Model Hysitron TI 725 Ubi., USA) test was conducted on the Ni-Co alloy deposited samples in a Ni70%-Co30% bath, by applying a load of 25 gf for 60 min to obtain thick deposits.

3. Results and discussion

3.1. Composition of the Ni-Co alloy

The relationship between the $[Co^{2+}]/[Ni^{2+}]$ ratio in the electrolytic solution and the cobalt content of the deposited Ni-Co alloys without and with additives, as well as the composition reference line (C.R.L.) is shown in S1. The C.R.L. is defined as follows:

$$(C.R.L.) = \frac{[Co^{2+}]}{[Co^{2+}] + [Ni^{2+}]} \times 100 \tag{1}$$

where $[Co^{2+}]$ and $[Ni^{2+}]$ denote the concentrations of Co and Ni in the electrolytes, respectively. S1 shows that in all the considered cases of the Ni-Co alloys obtained from the nine baths (listed in Table 1), the content of Co in the alloys (%), which is

a less noble metal, is always higher than that in the baths, and it lies above the C.R.L. The $[Co^{2+}]$ value in the electrolytes ranges from 30 g/L to 70 g/L, as indicated in Table 1, while the Co contents in the alloys, as determined in the EDS analysis, ranges from 38% to 79% when using the Ni-Co alloy deposited from IL free baths (bath 1, 4, and 7) as shown in Table 2 and S1 (red dots). These results indicate that Co is more readily deposited, and the reduction rate of the Co^{2+} ions is higher than that of the Ni^{2+} ions. Therefore, the codeposition of Co and Ni from the sulfate bath leads to anomalous plating. In the bath including 1×10^{-5} M of [MOFIM]I or [FPIM]Br, the anomalous behavior of the alloy deposition was alleviated. As indicated in S1 (green and blue dots) and Table 2, the Co content increased to maximum values of 85.33% and 83.62% in the presence of [MOFIM]I and [FPIM]Br, respectively. It is likely that the considered ILs favored the reduction of Co^{2+} over that of Ni^{2+}. i.e., the adsorption of the ILs at the cathode surface reduced the amount of simultaneous cathodic hydrogen discharge occurring during the Ni-Co alloy codeposition, thereby leading to a more effective Co deposition. The Co–Ni codeposition exhibited anomalous behavior when citrate (Lupi et al., 2017) and glycine (Al Radadi and Ibrahim, 2020) were added as complexing agents in the sulfate bath. The slight decrease in the percentage of Co deposited from bath 2 in the presence of [MOFIM]I could be attributed to an increase in the inhibition of the Co reduction at the expense of the reduction of Ni and hydrogen. This phenomenon probably occurred due to the high adsorption rate of [MOFIM]I on the surface of the cathode.

3.2. Cathodic current efficiency (CCE%)

The impact of the bath composition and plating operation conditions on the CCE was analyzed, and the results are present in Fig. 2 and Table 2. In all the experiments, the CCE% was slightly lower than 100% owing to the simultaneous H_2 evolution associated with the coating deposition process, as reported in (Al Radadi and Ibrahim, 2020). The presence of [MOFIM]I and [FPIM]Br considerably increased the CCE%, which exhibited maximum values of 99.8%, 97.91% and 97.76% in baths 2, 5 and 8, respectively, when using 1×10^{-5} M [MOFIM]I, as shown in Fig. 2b. Fig. 2c shows that the improvement in the CCE% was smaller when using [FPIM]Br (97.07%, 96.26% and 98.76% for baths 3, 6 and 9, respectively). The efficiency of the alloy codeposition improved in the presence of ILs due to the increase and

Table 2 C.R.L., Ni and Co contents in Ni-Co alloys and CCE% in absence and presence of [MOFIM]I and [FPIM]Br at optimum conditions.

	Ni70%-Co30%			Ni50%-Co50%				Ni30%-Co70%	
	Ni-Co1	Ni-Co2	Ni-Co3	Ni-Co4	Ni-Co5	Ni-Co6	Ni-Co7	Ni-Co8	Ni-Co9
(C.R.L.)	30	30	30	50	50	50	70	70	70
Co content (at%) EDX	38.03	35.55	48.96	59.80	65.65	60.76	79.09	85.33	83.62
Ni content (at%) EDX	59.54	63.23	58.76	37.68	31.84	36.11	14.55	11.48	13.69
CCE% Co	37.78	35.90	38.70	58.10	65.93	60.02	80.29	86.16	84.45
CCE% Ni	59.15	63.85	58.37	36.61	31.98	36.27	14.77	11.59	13.64
CCE% Ni-Co alloy	96.92	99.8	97.07	94.7	97.91	96.29	95.06	97.76	98.76

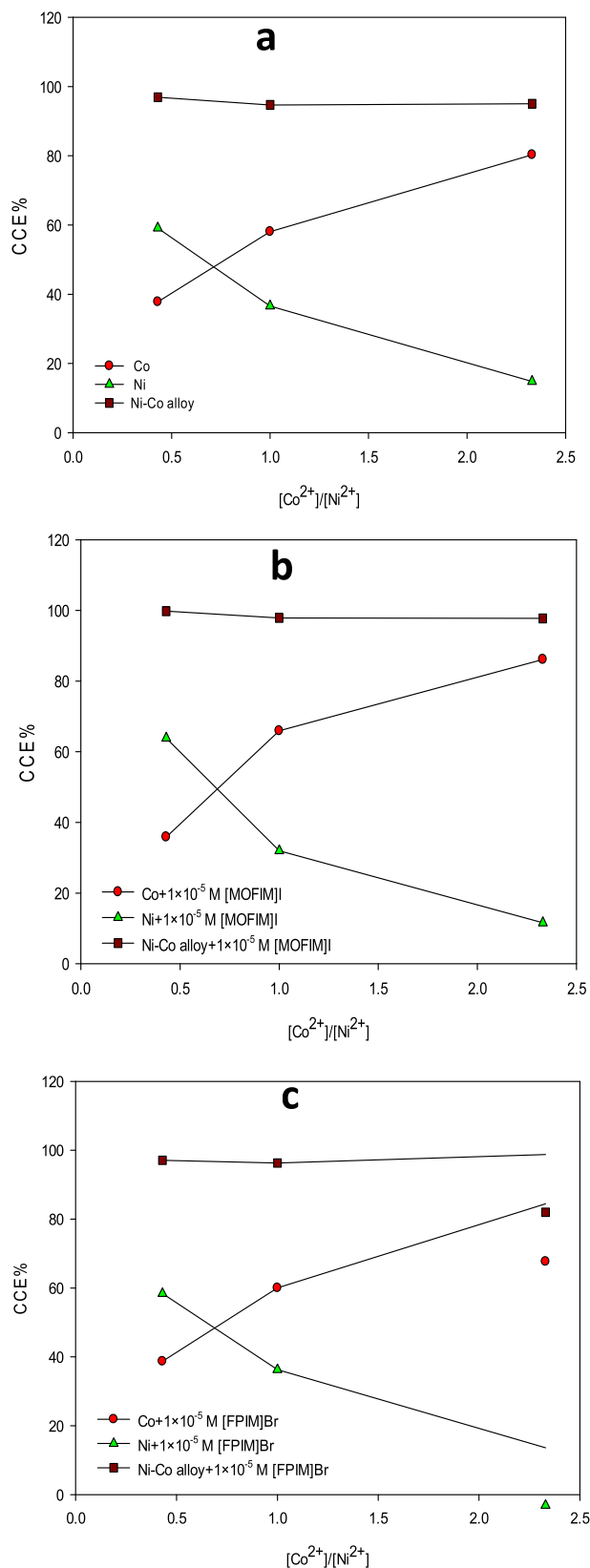**Fig. 2** Effect of $[Co^{2+}]/[Ni^{2+}]$ ratios in the bath on the CCE% of Ni-Co alloys deposits (a) Ni-Co1, Ni-Co4 and Ni-Co7 alloys (free IL), (b) Ni-Co2, Ni-Co5 and Ni-Co8 alloys (with 1×10^{-5} M [MOFIM]I), (c) Ni-Co3, Ni-Co6 and Ni-Co9 alloys (with 1×10^{-5} M [FPIM]Br), i = 20 mA cm^{-2}, t = 10 min., T = 25 °C.

decrease in the efficiency of the Co deposition and hydrogen evolution, respectively. According to the results presented in Table 2 and Fig. 2, the optimal bath composition for the Ni-Co alloy deposition, corresponding to the highest CCE% values, included 70 g/L and 30 g/L of Ni^{2+} and Co^{2+} concentrations, respectively, with the IL concentration as 1×10^{-5} M. The CCE% pertaining to the bath including [MOFIM]I was higher than that for the bath including [FPIM]Br owing to the stronger adsorption of the former molecule than the latter molecule on the cathode surface, which inhibited the hydrogen evolution. The Ni-Co alloy could be obtained with high current efficiencies (more than 95%) when using either [MOFIM]I or [FPIM]Br. When performing Ni-Co and codeposition from a sulfate bath using 1×10^{-5} M [MOFIM]I, the current efficiency value was nearly 100% compared to the CCE% values of 90% and 84.8% in the presence of sodium citrate (Lupi et al., 2017), glycine (Al Radadi and Ibrahim, 2020) respectively and CCE% values of Cu-Zn alloy about 68% in presence of polyethylene glycol (Ibrahim et al., 2019); Table 3.

3.3. Physical characterizations

Figs. 3–5 show SEM images of the Ni-Co alloys obtained from the nine baths. As shown in Fig. 3a and a', the surface morphology of the Ni-Co1 alloy obtained from a silent electrolyte (without ILs additive) in bath 1 was granulated and exhibited a lustrous structure despite the presence of many small (grain size 278 nm) and large circular grains (the maximum grain size 589 nm). The quality of the deposit was unsatisfactory due to the co-evolution of H_2 (Bahramian et al., 2018). The surface morphology of the alloy was enhanced significantly after 1×10^{-5} M [FPIM]Br was added, and the alloy became more compact and homogeneous; however, the presence of [MOFIM]I more effectively enhanced the Ni-Co2 alloy coating, as observed in Fig. 3b and b'. In particular, extremely few large grains were present in the Ni-Co3 alloy surface obtained using [FPIM]Br (the maximum grain size 225 nm), as shown in Fig. 3c and c'. In general, the [MOFIM]I and [FPIM]Br cations attach to the substrate and form layers through adsorption with a strong interaction (El-Feky et al., 2013). The ionic liquids undergo nonblocking adsorption in the active sites of the crystal planes of the substrates and on the emerging surfaces of the crystallizing phases (El-Feky et al., 2013) of the Ni-Co alloy. In other words, the ILs adsorb on the energetically favorable surfaces (low energy sites) on the substrate and the first stages of the Ni-Co alloy, which considerably inhibits the H_2 evolution, leading to pitting and cracking on the deposit surface. Consequently, only high energy sites are available for the metal deposition (Hashemi et al., 2017), and the ILs decelerate the surface diffusion of the adsorbed ion surface. This phenomenon impedes the grain growth, leading to a higher nucleation rate and the presence of finer grains, free cracks and more compact deposits. The deposits are compact as the deposits obtained in the presence of saccharin (Qibo and Yixin, 2017) and cysteine (El-Feky et al., 2013). The additives primarily occupy the active sites, which are the edges of a growth step, and the metal ions must form a new layer on the less active areas (El-Feky et al., 2013).

To further understand the role of the two studied ILs in enhancing the morphology of the Ni-Co alloy, as shown in

Table 3 Comparison of obtained results of Ni-Co2 and Ni-Co3 alloys coating in presence of 1×10^{-5} M [MOFIM]I and [FPIM]Br with other best bath composition in presence of additives.

Additives	CCE%	Ra	Microhardness (kg f mm^{-2})	Reference No.
[MOFIM]I	99.8	28.14 nm	852.5	Current work
[FPIM]Br	97.07	51.07 nm	775.0	Current work
Sodium citrate	90%	–	–	Lupi et al. (2017)
Glycine	84.8%	–	–	Al Radadi and Ibrahim (2020)
Polyethylene Glycol	68%	–	–	Kumar et al. (2019)
Fe^{2+}		–	510.0	Ji et al. (2016)
Fe^{2+} + H$_3$PO$_3$		–	690	Ji et al. (2016)
Fe		–	220	Deng et al. (2018)
Co		–	20	Deng et al. (2018)
Gd2O3 nanoparticles		–	590	Franklin (1987)
Ascorbic acid		0.389 μm	–	Budi et al. (2017)
Glycine		812.89 nm	–	Al Raddadi (2014)
Saccharin		266.96 nm	–	Tian et al. (2011)
Saccharin			280	Liu et al. (2019)

Fig. 1, the chemical composition of the two compounds was considered. [MOFIM]I and [FPIM]Br cations have a strongly cationic configuration, and thus, they readily adsorb on the cathode surface under an electric field. Specifically, $-C\equiv N-$, which is the functional group, and the electronegative nitrogen of imidazolium in both [MOFIM]I and [FPIM]Br cations enable the spontaneous adsorption of these ILs on the metal surface due to the specific interaction between these functional groups and the metal surface (Qibo and Yixin, 2017). Furthermore, the oxygen atoms in the amide and ether functional groups in the [MOFIM]I and [FPIM]Br structures, respectively, tend to donate electrons, which contributes to the strong adsorption ability of these ILs on the metal surface (Kumar et al., 2019). Moreover, both [MOFIM]I and [FPIM]Br molecules have double bonds in the aromatic rings in their structures. As the number of double bond increases, the number of π electrons increases, thereby facilitating the adsorption on the cathode surface (Deng et al., 2018). However, owing to the presence of an amide functional group in the [MOFIM]I structure, which contains highly electronegative nitrogen and oxygen atoms, this IL is a more effective additive compared to the [FPIM]Br.

When the Co^{2+} concentration in the bath increased to 50 g/L, the grain structure of Ni-Co4 changed from a circular to a starry shape with a maximum grain size of 691.7 nm, as shown in Fig. 4a and a'. The micrographs of the Ni-Co5 alloy indicate that after 1×10^{-5} M [MOFIM]I was added in bath 5, the starry shape changed to an elongated structure with needle-like crystals, which is not desirable for deposits, and the maximum grain size increased to 2.1 μm as shown in Fig. 4b and b'. Moreover, bath 6 including 1×10^{-5} M [FPIM]Br resulted in Ni-Co6, which exhibited undesirable sharp needlelike crystals with considerable elongation, distributed in completely random directions. Moreover, the maximum grain size increased to 2.8 μm, as shown in Fig. 4c and c'. A similar effect was noted when the ionic liquid 1-butyl-3-methylimidazolium hydrosulphate [BMIM]HSO$_4$ was used as an additive in the zinc electrodeposition process involving an acidic sulfate electrolyte (Qibo and Yixin, 2017).

With a further increase in the Co percentage, the Ni-Co7 alloy was deposited from an IL free bath (bath 7), and this alloy exhibited a granular, nodular, and spherical structure with cauliflower like grains, as shown in Fig. 5a and a'. A mixture of small and large grains was obtained, with the maximum grain size being 1.63 μm. When 1×10^{-5} M [MOFIM]I was added, in bath 8, the granular spherical grains of the alloy retained their shape, as shown in Fig. 5b and b'; however, the maximum grain size reduced to 1.03 μm. The presence of [MOFIM]I did not considerably influence the shape of the Ni-Co8 alloy obtained from bath 8. However, when 1×10^{-5} M [FPIM]Br was added in bath 9, as shown in Fig. 5c and c', the surface of the Ni-Co9 alloy became rough and exhibited fibril-like maximum grains sized 2.06 μm, which is not a preferable deposit quality. Increasing the Co content in the alloy composition led to larger grain structures. This phenomenon was especially notable in the cases with Ni50%-Co50% and Ni30%-Co70% baths, as the H$_2$ evolution increased owing to the higher overpotential, which is not desirable in the case of deposits. Granular Ni-Co alloys were also obtained from the silent bath (without ILs additive) due to the increase in the Co content in the Ni-Co alloys (El-Feky et al., 2013; Franklin, 1987). Moreover, a small valley was observed in Ni-Co7, Ni-Co8, Ni-Co9 alloys, which was similar to that observed in the of Ni-Co alloy morphology when the Co content in the alloys was more than 71% (El-Feky et al., 2013).

The elemental EDS mapping images shown in S2 indicate that the Ni and Co were uniformly distributed on the Cu substrate, even at a high magnification at which the crystallites could be clearly observed. This result suggests that Ni and Co are found within individual crystallite domains and confirms the formation of the Ni-Co solid solution, as shown in S2. a–c. The images also indicate the successful incorporation of the [MOFIM]I (S2. a'–c') and [FPIM]Br ILs (S2. a''–c'') into the Ni-Co film. The ILs exhibited a homogeneous distribution of the Ni and Co elements. A similar result has been reported for Ni-Co alloys deposited in the presence of saccharin (Budi et al., 2017), samarium oxide (Liu et al., 2019) and hydroxides (Chai and Jiang, 2019).
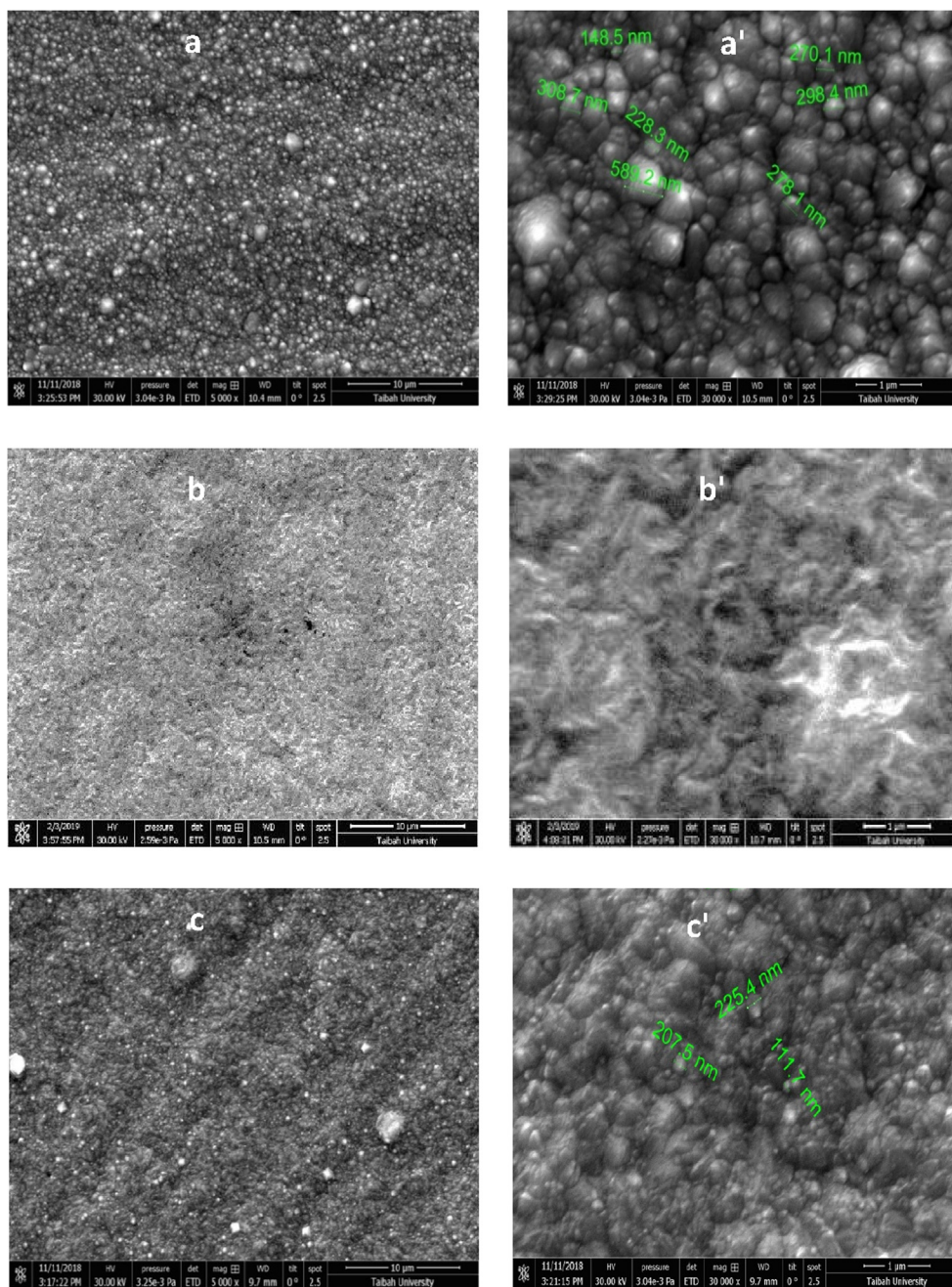
Fig. 3 SEM images, high magnification SEM of (a,a') Ni-Co1 alloy (free IL), (b,b') Ni-Co2, alloy (with 1×10^{-5} M [MOFIM]I), (c,c') Ni-Co3 alloy (with 1×10^{-5} M [FPIM]Br).

4. Analysis of the phase composition

Fig. 6 shows the XRD diagrams of the Cu substrate as well as the nine Ni-Co alloys electrodeposited from nine different bath compositions. The XRD patterns agree with the face center cubic (fcc) Cu substrate (JCPDS 00-004-0836) and Co-Ni (JCPDS 01-074-5694). The fcc structures of the Ni-Co alloys were not influenced by the change in the Ni^{2+} and Co^{2+} concentrations or the presence of [MOFIM]I and [FPIM]Br in the electrolytes, as shown in Fig. 6a–c. The only differences were in terms of the XRD peak intensity and width of the patterns. The XRD patterns of the Ni-Co1, Ni-Co2 and Ni-Co3 alloys

exhibited a large amount of (220), preferred growth orientation, and diminutive amounts of (111) and (200), as shown in Fig. 6a. Fig. 6b. shows that the XRD patterns of the Ni-Co7, Ni-Co8 and Ni-Co9 alloys were similar. Specifically, most of the alloy crystallites were oriented parallel to the (220) plane. The intensity of the Ni-Co (200) and (111) peaks changed slightly when [MOFIM]I and [FPIM]Br were introduced in the system. However, the XRD patterns of the Ni-Co4, Ni-Co5 and Ni-Co6 alloys exhibited diminutive amounts of fcc (220), (200) and (111). The introduction of [MOFIM]I and [FPIM]Br led to a significant and slight increase in the intensity of all the XRD pattern peaks of the Ni-Co5 and
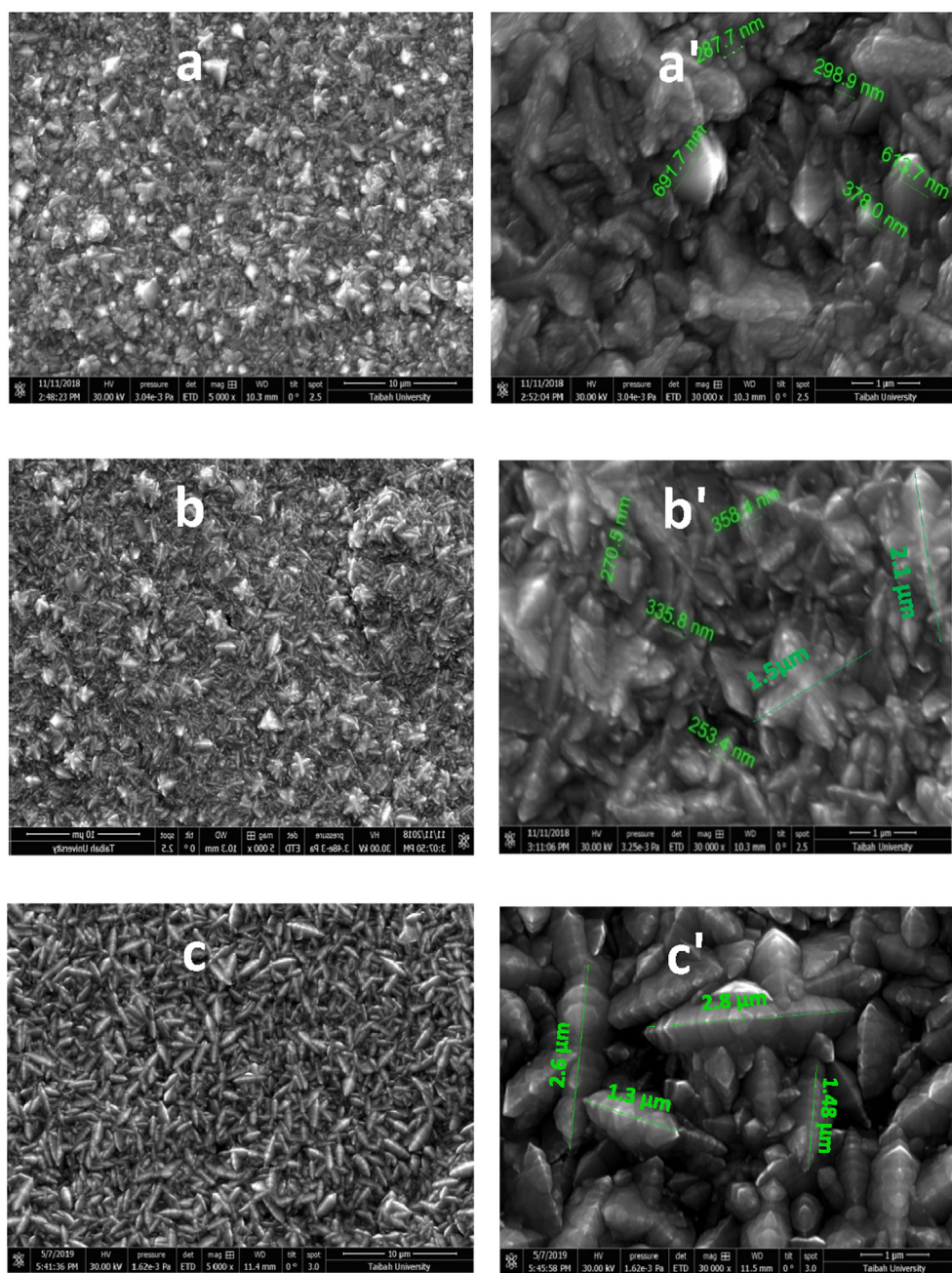
Fig. 4 SEM images, high magnification SEM of (a,a') Ni-Co4 alloy (free IL), (b,b') Ni-Co5, alloy (with 1×10^{-5} M [MOFIM]I), (c,c') Ni-Co6 alloy (with 1×10^{-5} M [FPIM]Br).

Ni-Co6 alloys, respectively, as shown in Fig. 6c. The average crystallite size of the fcc (2 2 0) of the Ni-Co2 film electrodeposited from bath 2 (including 1×10^{-5} M [MOFIM]I), calculated using the Scherrer equation, was 12.97 nm, which was significantly smaller than the corresponding values (15.54 and 17.63 nm, respectively) for the Ni-Co3 deposited using bath 3 with 1×10^{-5} M [FPIM]Br and Ni-Co1 deposited from IL free bath 1. This result indicates that [MOFIM]I could more effectively improve the surface morphology of the Ni-Co alloy deposits. The considerable decrease in the crystallite size in the presence of both the considered ILs could be due to an increase in the nucleation rate, which likely decreased the crystal growth rate during the deposition process. In general,

electrodeposition occurs through the nucleation of the crystallites on the substrate surface followed by their growth along with the formation of new nuclei (Budi et al., 2017). In the system containing [MOFIM]I and [FPIM]Br (baths 2 and 3, respectively), the cations of [MOFIM]I and [FPIM]Br could be absorbed on the active sites of the surface substrate, on which the metallic nuclei form and grow. This condition generated a physical barrier and impeded the kinetic transport at the electrolyte–electrode interface, thereby increasing the overpotential in the system, which favored the nucleation rate, as reported in (Budi et al., 2017), and suppressed the grain growth. This suppression could explain the small crystallite size in the Ni-Co2 and Ni-Co3 alloys. However, both the ILs
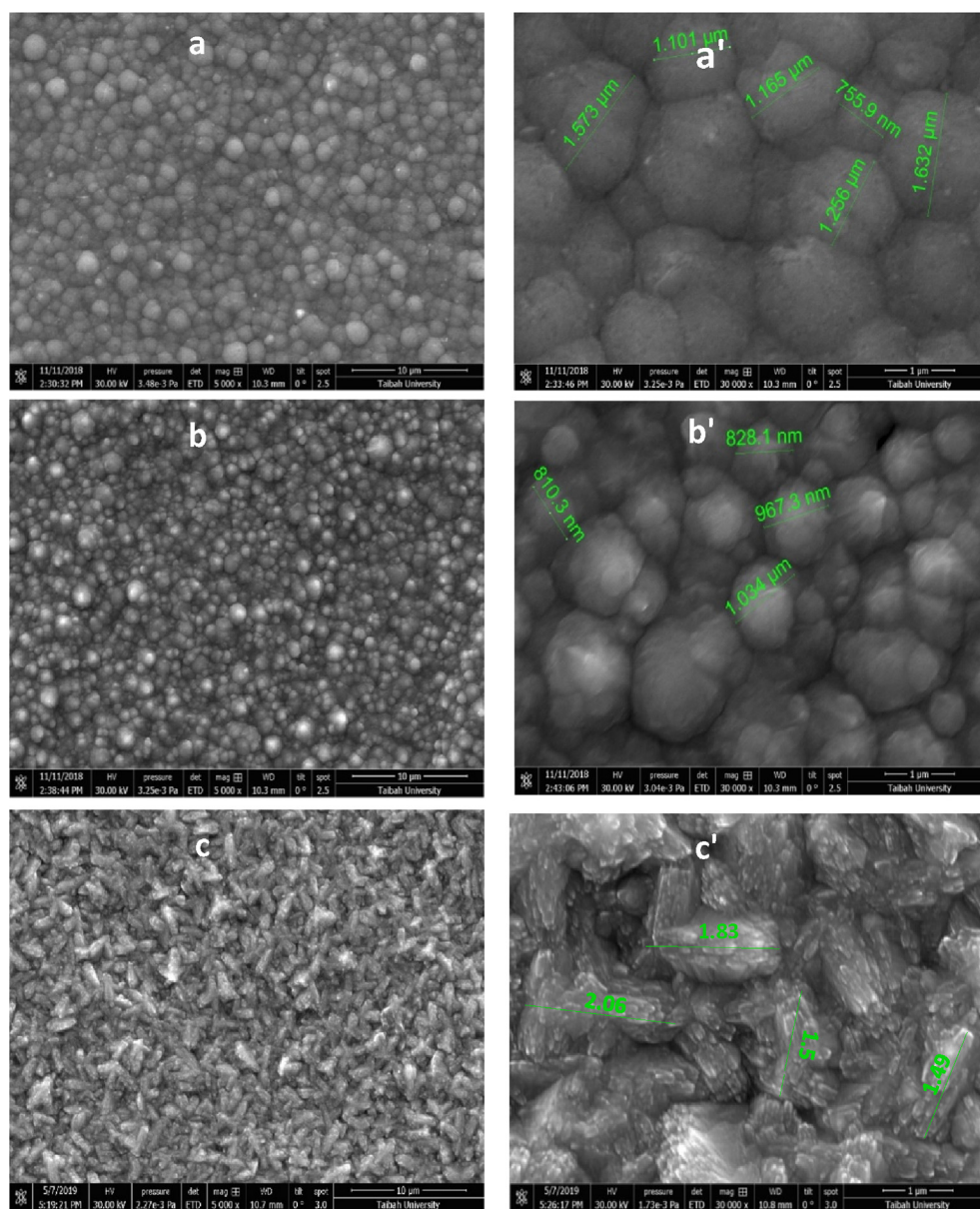
Fig. 5 SEM images, high magnification SEM of (a,a') Ni-Co7 alloy (free IL), (b,b') Ni-Co8, alloy (with 1×10^{-5} M [MOFIM]I), (c,c') Ni-Co9 alloy (with 1×10^{-5} M [FPIM]Br).

did not lead to a considerable enhancement in the Ni-Co8 and Ni-Co9 alloys, although [MOFIM]I was more effective than [FPIM]Br. The average crystallite sizes of the fcc (2 2 0) of the Ni-Co8 and Ni-Co9 films electrodeposited from baths containing [MOFIM]I and [FPIM]Br were 20.48 nm and 24.3 nm, respectively, which are slightly smaller than the corresponding value (25.45 nm) for Ni-Co7 deposited from free ILs.

5. Surface topography and roughness

The surface topography and roughness of the Cu substrate and Ni70%-Co30% bath coatings without and with different concentrations of [MOFIM]I and [FPIM]Br were investigated using the AFM technique. Fig. 7a and a' show the topography of the Cu substrate as 2D and 3D nuclei imaging in a flat sur-

face with low average roughness (R_a, deviation in height) and the total roughness (R_t, vertical distance between the deepest valley and highest peak (Emran and Al-Refai, 2017), respectively. The Ni-Co1 alloy deposited from the silent electrolyte (without ILs additive) in bath 1 exhibited a high roughness, as indicated by the large R_a (111.9 nm) and R_t (140.6 nm) values, as shown in Fig. 7b and b', respectively. This variation likely occurred due to the presence of randomly distributed and irregularly sized grain during co-electrodeposition due to the high polarization and co-evolution of H_2, as discussed in the SEM analysis. The lowest roughness (R_a of 28 nm and R_t of 35.5 nm) was obtained when [MOFIM]I was added in the system, as shown in Fig. 7c and c', respectively. Nevertheless, the coating quality was satisfactory in the case of [FPIM] Br (R_a of 51. 1 nm and R_t of 65.7 nm), as shown in Fig. 7d and d', respectively, although the efficiency in this case was lower
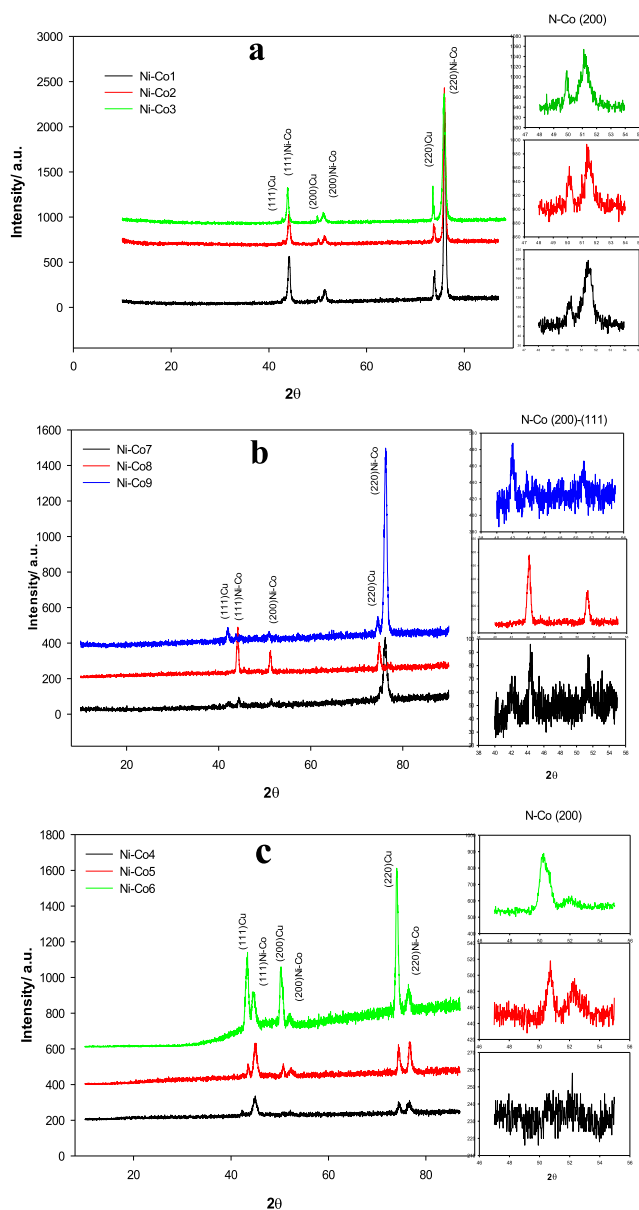
Fig. 6 XRD patterns of (a)Ni-Co1, Ni-Co2, Ni-Co3 alloys, (b) Ni-Co7, Ni-Co8, Ni-Co9 alloys, (c) Ni-Co4, Ni-Co5, Ni-Co6 alloys without and with 1×10^{-5}M [MOFIM]I and [FPIM]Br.

saccharin as the additive (Manhabosco and Müller, 2008) and glycine as the complexing agent (Al Raddadi, 2014) has been obtained during Co and Ni electrodeposition, Table 3.

6. Microhardness

The microhardness of the Ni-Co alloys obtained in the presence of [MOFIM]I and [FPIM]Br from baths 2 and 3, respectively, and from the silent electrolyte (without ILs additive) in the case of bath 1 was examined. The microhardness of the Ni-Co2 and Ni-Co3 alloys deposited in the presence of 1×10^{-5} M [MOFIM]I and [FPIM]Br was approximately 852.5 kg f mm^{-2} and 775 kg f mm^{-2}, respectively, compared to the microhardness of 541.75 kg f mm^{-2} of the Ni-Co1 alloy deposited from the silent bath. The hardness of the Ni-Co2 and Ni-Co3 alloys deposited in the presence of the two considered ILs was significantly increased compared to that of the Ni-Co1 deposit obtained in the absence of the ILs. Furthermore, [MOFIM]I was more efficient in increasing the hardness of the Ni-Co2 alloy film compared to [FPIM]Br. This phenomenon occurred because nanocoatings with smoother, more compact, denser and finer grains were obtained when using the [MOFIM]I and [FPIM]Br systems, as indicated by the SEM and XRD measurements. The hardening effect by the added agent can be attributed to the grain refinement effect. It has been reported that the mechanical properties of crystalline metals and alloys depend on the grain size (El-Feky et al., 2013). Consequently, the strength and hardness of a metallic material significantly increases when the grain size decreases. It is well-established that as the grain size of metal films increases, the surface roughness increases and metal hardness typically decreases (Pissolati and Majuste, 2018). Moreover, the microhardness of the Ni-Co alloys in the Ni70%-Co30% bath was affected by the crystal structure of the alloys, and the Ni-Co alloy with the fcc structure corresponded to a notably high hardness (El-Feky et al., 2013). It has been reported that Ni-Co alloy coatings exhibit a higher hardness with a higher Ni content in the alloys, owing to the formation of the solid solution of the Ni-Co alloys (El-Feky et al., 2013). Moreover, the microhardness values obtained in this study are considerably larger than those reported for Ni and Co alloys deposited under similar conditions (Ji et al., 2016; Oliveira et al., 2017; Sivasakthi and Sangaranarayanan, 2019); Table 3.

7. Conclusion

The surface morphology of Ni-Co alloy coatings was successfully enhanced by using 1-methyl-3-(2-oxo-2-((2,4,5trifluoro phenyl)amino)ethyle)-1H-imidazol-3-ium iodide [MOFIM]I and 1-(4-fluorobenzyl)-3-(4-phenoxybutyl)imidazol-3-ium bromide [FPIM]Br ionic liquids as additives in an acidic sulfate bath under three different [Ni²⁺] and [Co²⁺] concentrations. The addition of 1×10^{-5} M [MOFIM]I and [FPIM]Br in a bath with a composition of Ni70%-Co30% led to optimal Ni-Co alloy coatings, which exhibited characteristics such as finer grains, and a more coherent and compact deposit, as verified by SEM and AFM measurements. However, larger grains and more oriented crystals were obtained when using [MOFIM]I than when using [FPIM]Br. Both the considered ILs led to favorable results as they inhibited the Ni²⁺ and

than that with [MOFIM]I. This finding is in agreement with the more regular, compact and uniform alloy grain growth observed in the SEM images pertaining to the solution containing [MOFIM]I than that containing [FPIM]Br. Thus, lower concentrations (approximately 5×10^{-7} M) of both the considered ILs should be avoided as they lead to undesirably high roughness surfaces on the Ni-Co alloy deposits (R_a 105 nm, R_t 134.2 nm in the presence of [MOFIM]I; R_a 87.5 nm and R_t 111.6 nm in the presence of [FPIM]Br), as shown in Fig. 7e and e' and Fig. 7f and f', respectively. This phenomenon likely occurs owing to an increase in the activation overpotential of both the H_2 evolution and metal ions reduction, as reported in (Jamil et al., 2017). Moreover, this result is in agreement with the findings of the visual observation performed in the SEM analysis. A similar behavior of

Co^{2+} reduction owing to the adsorption of the IL cations on the energetically favorable surfaces on the substrate and the first stages of the Ni-Co alloy deposits. Owing to this adsorption, the ILs hindered the H_2 evolution, controlled the grain growth and increased the nucleation rate. The XRD spectra indicated that the addition of the considered ILs did not change the crystal structure of the co-electrodeposited Ni-Co alloys. In all the considered Ni-Co alloy coatings corresponding to baths 1–9, the Co content (the less noble metal) in the

alloy was higher than that in the bath, thereby indicating that the codeposition of Co and Ni corresponded to anomalous plating. The optimal bath conditions that led to the highest CCE% values for the co-electrodeposition of the Ni-Co alloys involved a current of 20 mA cm^{-2}, deposit potential of 6.5 V, pH of 4.5, temperature of 20 °C and deposit time of 10 min. The CCE% values attained maximum values of 99.8% and 97.07% in the presence of [MOFIM]I and [FPIM]Br, respectively, under the composition of Ni 70% and Co 30%.
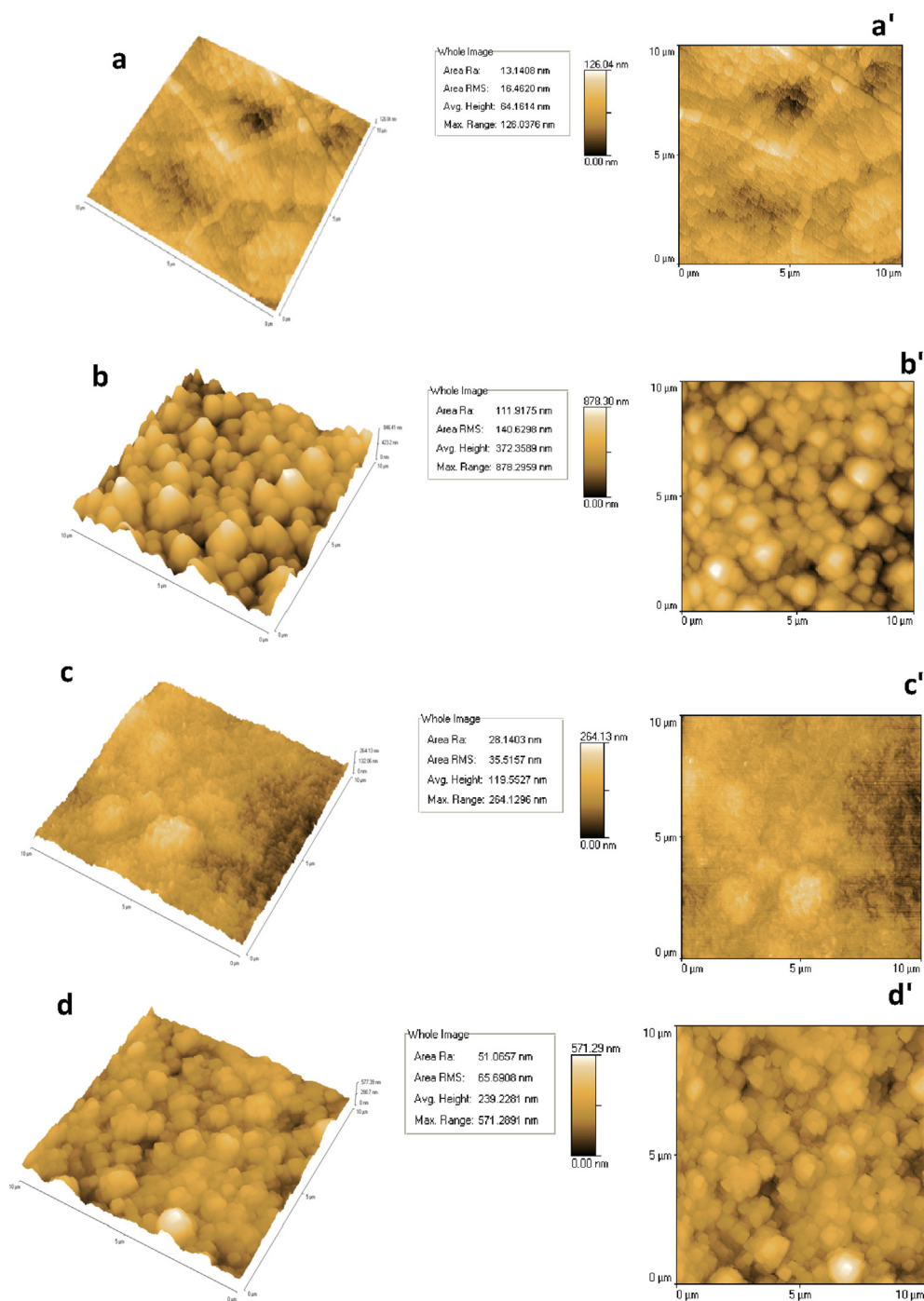

Fig. 7 AFM 3D, 2D images, of (a, a') Cu substrate, Ni-Co alloy deposits in (b, b') free ILs, with (c, c') 1×10^{-5} M [MOFIM]I, (d, d') 1×10^{-5} M [FPIM]Br, (e, e') 5×10^{-7} M [MOFIM]I, (f, f') 5×10^{-7} M [FPIM]Br.
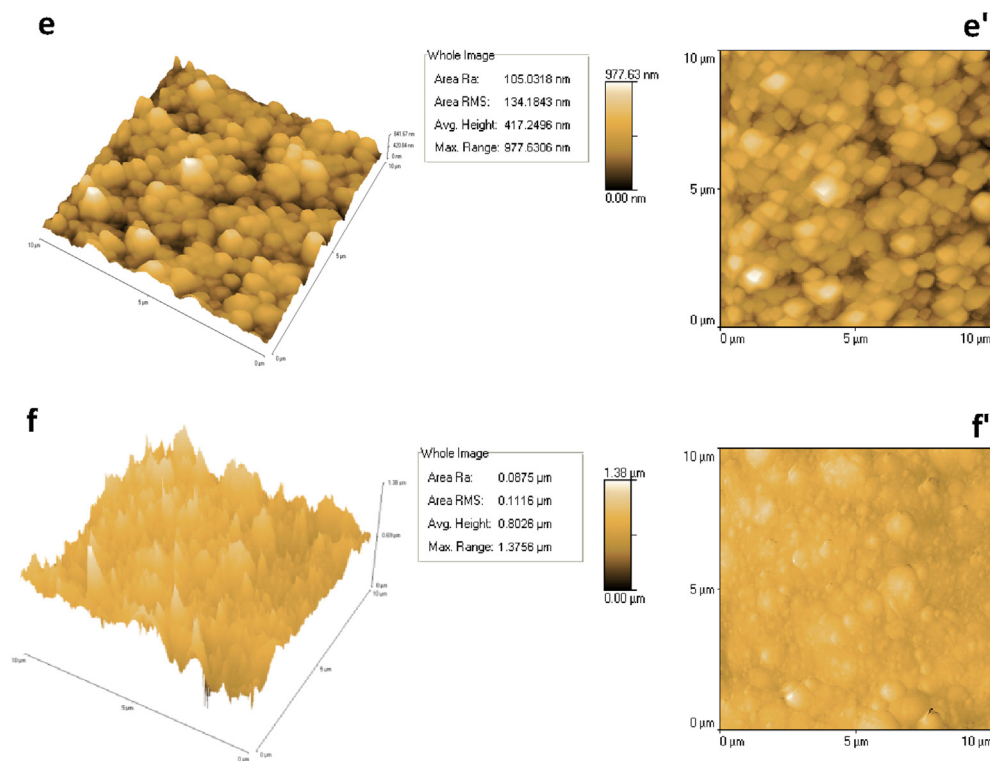
Fig. 7 (*continued*)

Declaration of Competing Interest

The authors declare that they have no known competing financial interests or personal relationships that could have appeared to influence the work reported in this paper.

Acknowledgments

Appendix A. Supplementary material

Supplementary data to this article can be found online at https://doi.org/10.1016/j.arabjc.2020.09.006.

References

Al Radadi, R.M., Ibrahim, M.A.M., 2020. Nickel-cobalt alloy coatings prepared by electrodeposition Part I : Cathodic current efficiency, alloy composition, polarization behavior and throwing power. Korean J. Chem. Eng. 37 (2), 1–10.

Al Raddadi, R.M., 2014. Cathodic codeposition of nickel-cobalt alloy coatings from acidic glycine complex baths. MS thesis, Taibah University, Faculty of Science.

Alesary, H.F., Cihangir, S., Ballantyne, A.D., Harris, R.C., Weston, D.P., Abbott, A.P., Ryder, S.R., 2019. Influence of additives on the electrodeposition of zinc from a deep eutectic solvent. Electrochim. Acta 304, 118–130.

Allahyarzadeh, M.H., Roozbehani, B., Ashrafi, A., 2011. Electrodeposition of high Mo content amorphous/nanocrystalline Ni–Mo alloys using 1-ethyl-3-methyl-imidazolium chloride ionic liquid as an additive. Electrochim. Acta 56 (27), 10210–10216.

Anicai, L., Florea, A., Visan, T., 2011. Studies regarding the nickel electrodeposition from choline chloride based ionic liquids. Applications of Ionic Liquids in Science and Technology. InTech.

Bahramian, A., Eyraud, M., Vacandio, F., Knauth, P., 2018. Improving the corrosion properties of amorphous Ni-P thin films using different additives. Surf. Coatings Technol. 345, 40–52.

Barbato, G., 2009. Electrodeposition of tantalum and niobium using ionic liquid.

Budi, S., Kurniawan, B., Mott, D.M., Maenosono, S., Umar, A.A., Manaf, A., 2017. Comparative trial of saccharin-added electrolyte for improving the structure of an electrodeposited magnetic FeCoNi thin film. Thin Solid Films 642, 51–57.

Cârâc, G., Ispas, A., 2012. Effect of nano-Al 2 O 3 particles and of the Co concentration on the corrosion behavior of electrodeposited Ni–Co alloys. J. Solid State Electrochem. 16 (11), 3457–3465.

Chai, Z., Jiang, C., 2019. Electrochemical/chemical growth of porous (Ni Co, Cu)(OH) 2 as an electrode material: Ternary Ni-Co-Cu nanocrystalline films corroded in neutral salt spray. Electrochim. Acta 294, 11–21.

Costovici, S., Manea, A.-C., Visan, T., Anicai, L., 2016. Investigation of Ni-Mo and Co-Mo alloys electrodeposition involving choline chloride based ionic liquids. Electrochim. Acta 207, 97–111.

Deng, J., Zhang, J., Tu, Y., Yang, P., An, M., Wang, P., 2018. Effect of BEO in the electrodeposition process of Ni/diamond composite coatings for preparation of ultra-thin dicing blades: experiments and theoretical calculations. Ceram. Int. 44 (14), 16828–16836.

El-Feky, H., Negem, M., Roy, S., Helal, N., Baraka, A., 2013. Electrodeposited Ni and Ni-Co alloys using cysteine and conventional ultrasound waves. Sci. China Chem. 56 (10), 1446–1454.

Emran, K.M., Al-Refai, H., 2017. Electrochemical and surface investigation of Ni-Cr glassy alloys in nitric acid solution. Int. J. Electrochem. Sci 12, 6404–6416.

Franklin, T.C., 1987. Some mechanisms of action of additives in electrodeposition processes. Surf. Coatings Technol. 30 (4), 415–428.

Hamilakis, S., Balgis, D., Milonakou-Koufoudaki, K., Mitzithra, C., Kollia, C., Loizos, Z., 2015. Electrodeposition of CdSe photoabsorber thin films in the presence of selected organic additives. Mater. Lett. 145, 11–14.

Hashemi, A.B., Kasiri, G., La Mantia, F., 2017. The effect of polyethyleneimine as an electrolyte additive on zinc electrodeposition mechanism in aqueous zinc-ion batteries. Electrochim. Acta 258, 703–708.

Ibrahim, S., Bakkar, A., Ahmed, E., Selim, A., 2016. Effect of additives and current mode on zinc electrodeposition from deep eutectic ionic liquids. Electrochim. Acta 191, 724–732.

Ibrahim, M.A.M., Omar, E.M.A., 2013. Synergistic effect of ninhydrin and iodide ions during electrodeposition of zinc at steel electrodes. Surf. Coatings Technol. 226, 7–16.

Ibrahim, M.A.M., Ismail, E.H., Bakdash, R.S., 2019. Copper-rich copper–zinc alloy coatings prepared by electrodeposition from glutamate complex electrolyte: current efficiency, Tafel kinetics and throwing power. Trans. IMF 97 (5), 237–246.

Ismail, A.S., 2017. Electrodeposition of aluminium–copper alloy from 1-butyl-1-methylpyrrolidinium bis (trifluoromethylsulfonyl) imide ionic liquid. Egypt. J. Pet. 26 (1), 61–65.

Jamil, Z., Ruiz-Trejo, E., Brandon, N.P., 2017. Nickel electrodeposition on silver for the development of solid oxide fuel cell anodes and catalytic membranes. J. Electrochem. Soc. 164 (4), D210–D217.

Ji, X., Yan, C., Duan, H., Luo, C., 2016. Effect of phosphorous content on the microstructure and erosion–corrosion resistance of electrodeposited Ni-Co-Fe-P coatings. Surf. Coatings Technol. 302, 208–214.

Kumar, U.P., Shanmugan, S., Kennady, C.J., Shibli, S.M.A., 2019. Anti-corrosion and microstructural properties of Ni–W alloy coatings: effect of 3, 4-Dihydroxybenzaldehyde. Heliyon 5 (3), 1–27.

Liu, H., Zeng, S., He, P., Dong, F., He, M., Zhang, Y., Wang, S., Li, C., Liu, M., Jia, L., 2019. Samarium oxide modified Ni-Co nanosheets based three-dimensional honeycomb film on nickel foam: a highly efficient electrocatalyst for hydrogen evolution reaction. Electrochim. Acta 299, 405–414.

Loto, C.A., 2012. Electrodeposition of zinc from acid based solutions: a review and experimental study. Asian J. Appl. Sci. 5 (6), 314–326.

Lupi, C., Dell'Era, A., Pasquali, M., 2017. Effectiveness of sodium citrate on electrodeposition process of NiCoW alloys for hydrogen evolution reaction. Int. J. Hydrogen Energy 42 (48), 28766–28776.

Manhabosco, T.M., Müller, I.L., 2008. Influence of saccharin on morphology and properties of cobalt thin films electrodeposited over n-Si (100). Surf. Coatings Technol. 202 (15), 3585–3590.

Mohanty, U.S., Tripathy, B.C., Singh, P., Das, S.C., 2002. Effect of $Cd2+$ on the electrodeposition of nickel from sulfate solutions.

Part I: Current efficiency, surface morphology and crystal orientations. J. Electroanal. Chem. 526 (1–2), 63–68.

Nemţoi, G., Chiriac, H., Dragoş, O., Apostu, M.-O., Lutic, D., 2009. The voltammetric characterization of the electrodeposition of cobalt, nickel and iron on gold disk electrode. Acta Chem. Iasi 17, 151–168.

Oliveira, R.P., Bertagnolli, D.C., Da Silva, L., Ferreira, E.A., Paula, A.S., Da Fonseca, G.S., 2017. Effect of Fe and Co co-deposited separately with Zn-Ni by electrodeposition on ASTM A624 steel. Appl. Surf. Sci. 420, 53–62.

Omar, I.M.A., Emran, K.M., Aziz, M., Al-Fakih, A.M., 2020. A novel viewpoint of an imidazole derivative ionic liquid as an additive for cobalt and nickel electrodeposition. RSC Adv. 10 (53), 32113–32126.

Omar, I.M.A., Aziz, M., Emran, K.M., 2020. Impact of Ionic Liquid [FPIM] Br on Electrodeposition of Ni and Co from Aqueous Sulfate Bath. no. submitted.

Omar, E.M.A., 2012. Effect of Organic Additives on Zinc Electrodeposition from Acidic Sulfate Bath. MS thesis, Taibah University, Faculty of Science.

Pissolati, N.C., Majuste, D., 2018. Morphology, roughness and microhardness of nickel electrodeposits produced in sulfate media on 316 L SS or Ti cathodes. Hydrometallurgy 175, 193–202.

Qibo, Z., Yixin, H., 2017. Ionic liquids as electrodeposition additives and corrosion inhibitors. Progress and Developments in Ionic Liquids. InTech.

Rezki, N., Al-blewi, F.F., Al-Sodies, S.A., Alnuzha, A.K., Messali, M., Ali, I., Aouad, M.R., 2020. Synthesis, characterization, DNA binding, anticancer, and molecular docking studies of novel imidazolium-based ionic liquids with fluorinated phenylacetamide tethers. ACS Omega.

Sivasakthi, P., Sangaranarayanan, M.V., 2019. Influence of pulse and direct current on electrodeposition of NiGd2O3 nanocomposite for micro hardness, wear resistance and corrosion resistance applications. Compos. Commun. 13, 134–142.

Tian, L., Xu, J., Xiao, S., 2011. The influence of pH and bath composition on the properties of Ni–Co coatings synthesized by electrodeposition. Vacuum 86 (1), 27–33.

Vijayakumar, J., Mohan, S., Kumar, S.A., Suseendiran, S.R., Pavithra, S., 2013. Electrodeposition of Ni–Co–Sn alloy from choline chloride-based deep eutectic solvent and characterization as cathode for hydrogen evolution in alkaline solution. Int. J. Hydrogen Energy 38 (25), 10208–10214.

Yao, K., Zhai, M., Ni, Y., 2019. α-Ni (OH) 2· 0.75 H2O nanofilms on Ni foam from simple NiCl2 solution: Fast electrodeposition, formation mechanism and application as an efficient bifunctional electrocatalyst for overall water splitting in alkaline solution. Electrochim. Acta 301, 87–96.

Zamani, M., Amadeh, A., Baghal, S.M.L., 2016. Effect of Co content on electrodeposition mechanism and mechanical properties of electrodeposited Ni–Co alloy. Trans. Nonferrous Met. Soc. China 26 (2), 484–491.

Zhu, Y.-L., Katayama, Y., Miura, T., 2012. Effects of acetone and thiourea on electrodeposition of Ni from a hydrophobic ionic liquid. Electrochim. Acta 85, 622–627.